Arabian Journal for Science and Engineering
https://doi.org/10.1007/s13369-025-11013-z

RESEARCH ARTICLE-MECHANICAL ENGINEERING

Utilizing Response Surface Methodology (RSM) on Magnetohydrodynamic Ternary Nanofluid Flow Over a Radiated Nonlinearly Permeable Shrinking Sheet for Heat Transfer Optimization

Shahirah Abu Bakar[1] · Nur Syahirah Wahid[2] · Norihan Md Arifin[2,3] · Ioan Pop[4]

Received: 3 March 2025 / Accepted: 11 December 2025

Abstract

A nonlinear permeable shrinking sheet refers to a boundary where the permeability changes nonlinearly, and the sheet itself is contracting or shrinking over time. Meanwhile, magnetohydrodynamics (MHD) models electrically conducting fluids as a single continuous medium. Hence, this research integrates magnetohydrodynamics (MHD) models electrically conducting fluids as a single continuous medium. The distribution of three nanoparticles—aluminum oxide (Al_2O_3), titanium dioxide (TiO_2), and silver (Ag)—in water (H_2O) is considered to represent the ternary nanofluid model. Two analyses are performed: (i) numerical analysis—to describe the mathematical model; and (ii) statistical analysis—to optimize the heat transfer rate using Response Surface Methodology (RSM). The numerical results are obtained through bvp4c scheme in MATLAB after applying similarity transformation to reduce the governing equations. The findings show dual solutions due to the shrinking parameter, while ternary nanoparticles enhance heat transfer more than mono- or hybrid nanofluids. The nonlinearity parameter increases temperature profiles, whereas heat generation decreases them. Further, Response Surface Methodology (RSM) is applied to optimize the highest heat transfer rate by identifying three optimal parameter values for nonlinearity, radiation, and heat generation. With a suggested desirability of 99.98%, the optimization approach suggests that minimizing nonlinearity while maximizing radiation and heat generation parameters leads to the highest heat transfer rate. Potential applications of this work can consider systems with thermal management such as high-temperature furnaces, or high-performance coatings for aerospace surfaces that exposed to radiative and electromagnetic effects.

Keywords Ternary nanofluid · Nonlinearity · Optimization · Response surface methodology · Heat transfer rate

1 Introduction

Nanofluids consist of nanoparticles dispersed in a base fluid, a concept introduced by Choi and Eastman in 1995 [1]. Adding nanoparticles such as carbon nanotubes or metal oxides to base fluids significantly improves heat transfer capacity and thermal characteristics, as these fluids brings better thermo-physical properties than classic fluids. Huminic and Huminic [2] reviewed recent studies on the thermophysical properties of hybrid nanofluids, as well as their heat transfer and flow behavior in different heat exchangers. Findings show that hybrid nanofluids improve thermal conductivity and enhance heat transfer in these systems. Both experimental and numerical studies further confirm that hybrid nanofluids play a significant role in boosting heat transfer efficiency. However, more research is needed to study different combinations of hybrid nanoparticles, their mixing ratios, the stability of hybrid nanofluids, and the mechanisms that contribute to heat transfer enhancement and efficiency, which later is improved by adding a third type of nanoparticle. The evolution of these nanofluids aims to optimize the fluid performance for specific applications in electronics cooling, automotive cooling systems, or spinning disk reactor [3,

✉ Shahirah Abu Bakar
shahirah.abubakar@utm.my

1 Takasago Thermal/Environmental Systems Laboratory, Malaysia-Japan International Institute of Technology, Universiti Teknologi Malaysia, 54100 Kuala Lumpur, Malaysia

2 Department of Mathematics and Statistics, Faculty of Science, Universiti Putra Malaysia, 43400 Serdang, Selangor, Malaysia

3 Institute for Mathematical Research, Universiti Putra Malaysia, 43400 Serdang, Selangor, Malaysia

4 Department of Mathematics, Babes-Bolyai University, 400084 Cluj-Napoca, Romania

Published online: 05 January 2026

4]. The evolution toward ternary hybrid nanofluids, such as those composed of aluminum oxide (Al_2O_3), titanium dioxide (TiO_2), and silver (Ag), aims to capitalize on the unique properties of each nanoparticle to achieve superior thermal performance. As such, Ag offers excellent thermal conductivity, though they are expensive and can lead to potential agglomeration issues. TiO_2 nanoparticles are known for their stability and high refractive index, but they exhibit lower thermal conductivity compared to Ag. On the other hand, Al_2O_3 nanoparticles are cost-effective and provide good thermal conductivity and chemical stability, but they may not match the thermal performance of Ag. However, the complexity of such a system may also pose challenges, including potential difficulties in maintaining uniform dispersion, controlling viscosity, and ensuring long-term stability of the suspension [5, 6]. Mahmood et al. [7] studied the impact of heat generation and velocity slip on a stagnation point flow of tri-hybrid nanofluid near a shrinking sheet. Their findings showed that the ternary nanofluid resulted in the highest skin friction coefficient and heat transfer rates compared to the other two types of nanofluids. Nasir et al. [8] studied a nonlinear convection and radiation on ternary hybrid nanofluids past a stretchable surface, while a magnetized ternary hybrid nanofluid flow with nanoparticle shape has been numerically discussed by Shanmugapriya et al. [9]. They found that the blade-shaped nanoparticles achieved the highest heat transfer rate, which was significantly greater than that of hybrid nanofluids. Gohar et al. [10] investigated tri-hybrid nanofluid flow with nonlinear radiation over a spinning disk, highlighting its relevance to energy use in technical and industrial applications. Further, Madhukesh et al. [11] examined the thermal performance of ternary hybrid nanofluid flow over an inclined plate and a cylinder, reporting an increase in heat distribution from 2.08 to 2.32% for the cylinder and from 5.19% to 10.83% for the plate. Additional studies on ternary nanofluids can be found in the works of Sarangi et al. [12] and Mohanty et al. [3].

A nonlinearly shrinking sheet refers to a surface that contracts in a nonlinear manner as it moves in the direction of the flow. Unlike a linear shrinking sheet, the rate of contraction for nonlinear shrinking sheet changes according to a nonlinear function of position or time [13]. The concept of this interest has applications in fields such as polymer processing, cooling process of electronic devices, as well as pumps and generators, since nonlinear shrinking sheet provides a more accurate representation of how surfaces interact with fluids and improved the control over processing the heat transfer. By integrating nonlinear effects, engineers and scientists can better optimize performance and efficiency in various applications [14]. As such, Zaimi et al. [15] developed a model of nanofluid flow over a nonlinearly permeable stretching/shrinking sheet, while Khan et al. [16] performed on a nanofluid flow past a nonlinearly stretching/shrinking wedge with MHD and radiation. A study of hybrid nanofluid flow past a nonlinearly permeable stretching and shrinking surfaces with radiation has been initiated by Waini et al. [17] and Lund et al. [18] then studied a three-dimensional rotating flow of hybrid nanofluid past a nonlinearly shrinking sheet with MHD. To date, several researchers have expressed interest in nonlinearly shrinking sheet and have conducted studies on them [19–21]. Further, velocity slip in boundary layer represents an important aspect of fluid dynamics that can be leveraged to improve the performance of various industrial devices and applications. In boundary layer studies, velocity slip defines as the velocity of a fluid near a solid surface that deviates from that predicted by no-slip boundary conditions, where the no-slip condition assumes that the fluid velocity at the solid boundary is zero [22]. However, in certain practical situations, this assumption may not hold true due to various factors such as surface roughness, surface coating, or the presence of nanoscale features. The velocity slip then occurs when the fluid molecules near the solid boundary experience reduced frictional drag, compared to what is predicted by the no-slip condition, as explained by Sahraoui and Kaviany [23]. One such example of velocity slip in applications is in nanofluidic systems that is used for DNA sequencing [24]. To determine the fluid behavior, velocity slip effects allow researchers to design novel nanofluidic channels and devices with tailored fluidic properties, which enabling precise control over fluid flow and particle transport. Manjunatha et al. [25] developed a work on slip effects through the blood flow past a bi-directional stretching sheet by following the model of tri-hybrid nanofluid, while Rafique et al. [26] performed the effects of velocity slip and variable viscosity on ternary Al_2O_3-Cu-TiO_2/H_2O nanofluid over a disk surface. Another study of tri-nanofluid flow with linear radiation and slip flow has been assessed by Sudharani et al. [27] and their analysis showed the decaying of velocity profiles in ternary hybrid nanofluid flow when the nanoparticle value improved. In comparison with tri-hybrid and hybrid nanofluid, the ternary nanomaterial showed to possess the higher heat transfer rate. Recently, another comprehensive study by Mumtaz et al. [28] showed that a substantial impact on thermal conductivity by the nanoparticle volume fraction. Based on this report, a 1% increase in volume fraction improves the thermal conductivity by 6%, whereas this figure rises to 26% when the value of fraction reaches 4%.

Building on the reviewed literature, this research examines the theoretical aspects of magnetohydrodynamics (MHD), velocity slip, thermal radiation, and heat generation in a ternary nanofluid flow over a nonlinearly permeable shrinking sheet. While previous studies have explored nanofluids in different flow configurations, research on ternary nanofluid flow over a nonlinearly shrinking sheet remains limited. In particular, there is a lack of studies that apply an optimization approach to improve heat transfer performance in this

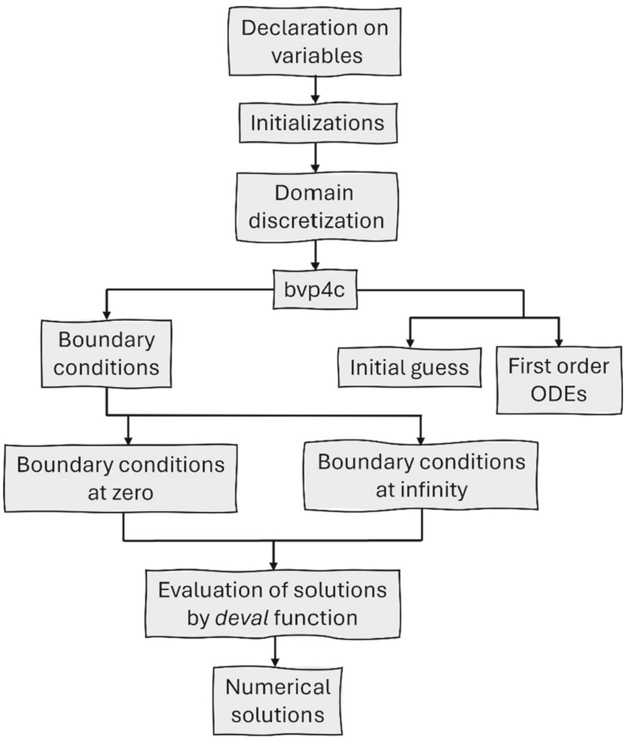

Fig. 1 The bvp4c process for the numerical analysis

setting. This research then addresses that gap by focusing on optimizing heat transfer using the Response Surface Methodology (RSM). This combined approach highlights both flow behavior and optimal thermal performance particular on the nonlinearly shrinking surface, which has not been reported in earlier studies. Further, the study has three main objectives: (i) to formulate and model the mathematical equations based on the problem framework, (ii) to analyze how different parameters affect ternary nanofluid flow over a nonlinearly shrinking sheet, and (iii) to determine the best combination of three parameters value to maximize heat transfer.

The method of this research brings to two analyses: (i) numerical, and (ii) statistical. For the mathematical model, a similarity transformation technique is applied to convert the nonlinear partial differential equations (PDEs) into a system of nonlinear ordinary differential equations (ODEs). Numerical analysis is then carried out using MATLAB's bvp4c function. This solver requires defining the differential equations, boundary conditions, and initial guesses, and it iteratively refines the solution until it satisfies both the ODEs and boundary conditions. This makes it a valuable tool for solving a wide range of boundary value problems (BVPs) arising in various scientific and engineering applications [29]. Figure 1 outlines the process of algorithm used in this solver.

For the optimization process, nonlinearity, radiation, and heat generation parameters are selected, and RSM is applied using Minitab software to determine their optimal values for achieving the maximum rate of heat transfer. The outcomes of this research, derived from both numerical and statistical analyses, hold potential applications in advanced energy systems requiring efficient heat and thermal management.

2 Formulation of Mathematical Model

2.1 Governing Equations

The formulation of this problem is based on several physical and mathematical assumptions to simplify the governing equations and describe the flow system clearly, as depicted in Fig. 2. These assumptions are listed below in chronological order:

- The flow is steady, two-dimensional, and incompressible.
- The fluid electrically conducting and influence by a uniform transverse magnetic field of strength B_0 applied along the y-direction.
- The sheet is located at $y = 0$, with the flow taking place in the region $y \geq 0$.
- Cartesian coordinates x, y are defined such that the x-axis lies along the sheet, and the y-axis is normal to it.
- The sheet moves with velocity $u = u_w(x)\Gamma + u_{slip}(x)$, where $\Gamma > 0$ indicates stretching, $\Gamma < 0$ denotes shrinking, and $\Gamma = 0$ is a static sheet.
- Velocity slip at the surface is considered by $u_{slip}(x)$.
- The surface temperature is defined as $T_w(x) = T_\infty + T_0 \left(\frac{x}{l}\right)^m$, where T_0 is the characteristic temperature, l is the characteristic length, T_∞ is the far-field temperature, and m is the nonlinear boundary condition for surface temperature when $m \neq 0$ and $m \neq 1$.
- Effects of thermal radiation and volumetric heat generation are included.
- The nanoparticles of Al_2O_3, TiO_2, and Ag are assumed to be uniformly dispersed, with no slip between the base fluid and nanoparticles.
- Fluid properties are assumed to be constant, except for the density variation in the buoyancy term (Boussinesq approximation).
- The flow is confined within the boundary layer regime, and external forces other than the applied magnetic field are neglected.

Based on these assumptions, the boundary layer equations for continuity, momentum, and energy governing the ternary nanofluid flow, which follow a quadratic form, can be expressed in Cartesian coordinates (x, y) as [30]

$$\frac{\partial u}{\partial x} + \frac{\partial v}{\partial y} = 0 \tag{1}$$

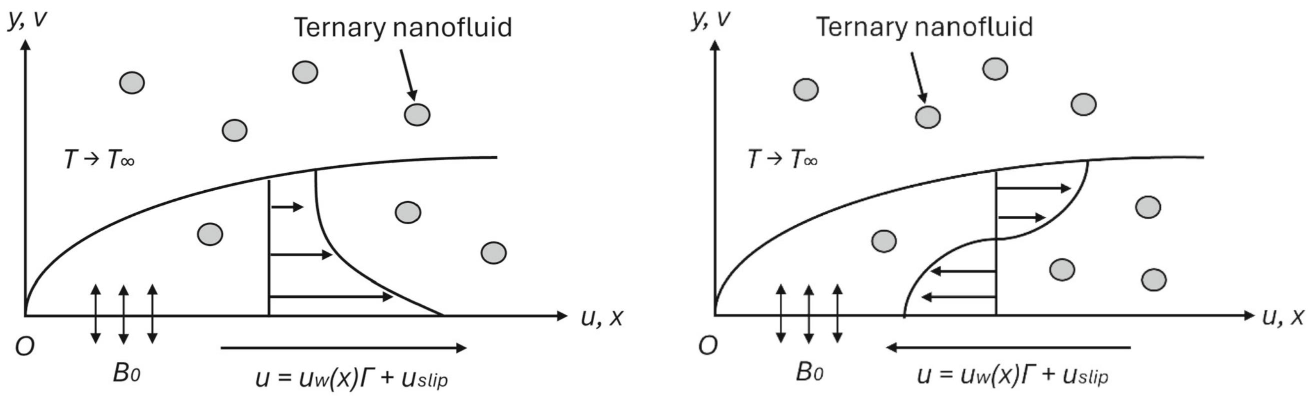

(a) Stretching sheet

(b) Shrinking sheet

Fig. 2 Coordinate system for two surfaces

$$u\frac{\partial u}{\partial x}+v\frac{\partial u}{\partial y}=\frac{\mu_{thnf}}{\rho_{thnf}}\frac{\partial^2 u}{\partial y^2}-\frac{\sigma_{thnf}}{\rho_{thnf}}B_0^2 u$$
$$v=v_w(x),\ u=ax\Gamma+L_1(x)\frac{\partial u}{\partial y}\text{ at }y=0 \tag{2}$$
$$u=u_e(x)\to 0\text{ as }y\to\infty$$

$$\begin{aligned}u\frac{\partial T}{\partial x}+v\frac{\partial T}{\partial y}=&\frac{k_{hnf}}{(\rho C_p)_{hnf}}\frac{\partial^2 T}{\partial y^2}+\frac{\mu_{hnf}}{(\rho C_p)_{hnf}}\left(\frac{\partial u}{\partial y}\right)^2\\&+\frac{\sigma_{hnf}}{(\rho C_p)_{hnf}}B_0^2u^2-\frac{1}{(\rho C_p)_{hnf}}\frac{\partial q_r}{\partial y}\\&+\frac{Q_0(T-T_\infty)}{(\rho C_p)_{hnf}}\\T&=T_w(x)+T_0(x)^m\text{ at }y=0\\T&\to T_\infty\text{ as }y\to\infty\end{aligned} \tag{3}$$

Here, u and v are the velocity components of the ternary nanofluid flow along the x and y axes, respectively, and T is the temperature. Further, parameter a is constant, L_1 is the velocity slip factor, Q_0 is heat generation coefficient, and q_r is the radiative heat flux which expressed by

$$q=-\frac{4\sigma*}{3k*}\frac{\partial T^4}{\partial y} \tag{4}$$

where $k*$ is the coefficient of mean absorption and $\sigma*$ is the Stefan-Boltzmann constant. The expression for q_r can be simplified to $T^4\approx 4T_\infty^3(T-3T_\infty^4)$ by ignoring higher-order terms and expanding T^4 using a Taylor series around the far field T_∞. The symbol μ, k, ρ, σ, and (ρC_p) are represented as the ternary nanofluid's dynamic viscosity, thermal conductivity, density, electrical conductivity, and heat capacitance, respectively. Additionally, Tables 1 and 2 provide the property correlations and thermophysical characteristics for three nanoparticles namely Al_2O_3 (φ_1), TiO_2 (φ_2), and Ag (φ_3).

2.2 Mathematical Solutions

According to Waini et al. [17] and Obalalu et al. [33], the following dimensionless variables can be introduced by

$$\begin{aligned}&u=ax^m f'(\eta),\\&v=-\left[\frac{(m+1)av_f}{2}\right]^{1/2}x^{(m-1)/2}\left[f(\eta)+\frac{m-1}{m+1}\eta f'(\eta)\right],\\&\theta(\eta)=\frac{T-T_\infty}{T_w(x)-T_\infty},\ \eta=y\sqrt{\frac{(m+1)a}{\nu_f}}x^{(m-1)/2}\end{aligned} \tag{5}$$

so that

$$v_w(x)=-\left[\frac{(m+1)a\nu_f}{2}\right]^{1/2}x^{(m-1)/2}S \tag{6}$$

and

$$L_1(x)=x^{(m-1)/2}L \tag{7}$$

where η is a dimensionless similarity variable and L is velocity slip parameter. From Eq. (6), S is suction parameter being that $S>0$. Otherwise, $S<0$ represents injection parameter while $S=0$ is impermeable condition.

The following BVPs can finally be obtained by configuring Eq. (5) with Eqs. (2) and (3) via a similarity transformation technique, which listed below as

$$\frac{\mu_{thnf}/\mu_f}{\rho_{thnf}/\rho_f}f'''-\frac{2m}{m+1}f'^2-\frac{\sigma_{thnf}/\sigma_f}{\rho_{thnf}/\rho_f}Mf\prime+ff''=0 \tag{8}$$

Table 1 Properties relationship for ternary nanofluid [31]

Properties	Ternary nanofluid
Dynamic viscosity	$\mu_{thnf} = \frac{\mu_f}{(1-\varphi_1)^{2.5}(1-\varphi_2)^{2.5}(1-\varphi_3)^{2.5}}$
Density	$\rho_{thnf} = (1-\varphi_3)\{(1-\varphi_2)[(1-\varphi_1)\rho_f + \varphi_1\rho_1] + \varphi_2\rho_2\} + \varphi_3\rho_3$
Thermal capacity	$(\rho C_p)_{thnf} = (1-\varphi_3)\left\{\begin{array}{l}(1-\varphi_2)[(1-\varphi_1)(\rho C_p)_f + \varphi_1(\rho C_p)_1] \\ +\varphi_2(\rho C_p)_2\end{array}\right\} + \varphi_3(\rho C_p)_3$
Thermal conductivity	$\frac{k_{nf}}{k_f} = \frac{k_1+2k_f-2\varphi_1(k_f-k_1)}{k_1+2k_f+\varphi_1(k_f-k_1)}$
	$\frac{k_{hnf}}{k_{nf}} = \frac{k_2+2k_{nf}-2\varphi_2(k_{nf}-k_2)}{k_2+2k_{nf}+\varphi_2(k_{nf}-k_2)}$
	$\frac{k_{thnf}}{k_{hnf}} = \frac{k_3+2k_{hnf}-2\varphi_3(k_{hnf}-k_3)}{k_3+2k_{hnf}+\varphi_3(k_{hnf}-k_3)}$
Electrical conductivity	$\frac{\sigma_{nf}}{\sigma_f} = \frac{\sigma_1+2\sigma_f-2\varphi_1(\sigma_f-\sigma_1)}{\sigma_1+2\sigma_f+\varphi_1(\sigma_f-\sigma_1)}$
	$\frac{\sigma_{hnf}}{\sigma_{nf}} = \frac{\sigma_2+2\sigma_{nf}-2\varphi_2(\sigma_{nf}-\sigma_2)}{\sigma_2+2\sigma_{nf}+\varphi_2(\sigma_{nf}-\sigma_2)}$
	$\frac{\sigma_{thnf}}{\sigma_{hnf}} = \frac{\sigma_3+2\sigma_{hnf}-2\varphi_3(\sigma_{hnf}-\sigma_3)}{\sigma_3+2\sigma_{hnf}+\varphi_3(\sigma_{hnf}-\sigma_3)}$

Table 2 Properties of water and three nanoparticles [5, 32]

Physical properties	Al_2O_3	TiO_2	Ag	H_2O
$\rho(\text{kg/m}^3)$	3970	4250	10,500	997.1
C_p(J/kg K)	765	686.2	235	4179
k (W/mK)	40	8.9538	429	0.613
σ (S/m)	35×10^6	2.38×10^6	6.3×10^7	5.5×10^{-6}

$$\frac{1}{\Pr}\frac{1}{(\rho C_p)_{thnf}/(\rho C_p)_f}\left(\frac{k_{thnf}}{k_f} + \frac{4}{3}R\right)\theta'' + \frac{Ec}{m+1}\left(f''^2 + \frac{\sigma_{thnf}/\sigma_f}{\mu_{thnf}/\mu_f}Mf'^2\right) - \frac{2m}{m+1}f'\theta + f\theta' + Q\theta = 0 \tag{9}$$

bound to

$$\begin{aligned} &f(0) = S,\ f'(0) = \Gamma + Lf''(0),\ \theta(0) = 1 \\ &f'(\eta) \to 0,\ \theta(\eta) \to 0 \text{ as } \eta \to \infty \end{aligned} \tag{10}$$

The respective parameters in Eqs. (8) – (10) are then defined as

$$\begin{aligned} &M = \frac{\sigma_f B_0^2}{a\rho_f},\ \Pr = \frac{(\rho C_p)_f}{k_f},\ R = \frac{4\sigma * T_\infty^3}{k * k_f}, \\ &Ec = \frac{u_w^2}{C_p[T_w(x) - T_\infty]}, \\ &L = \sqrt{\frac{(m+1)al^2}{\nu_f}},\ Q = \frac{Q_0}{(m+1)a} \end{aligned} \tag{11}$$

where M is magnetic parameter, Pr is Prandtl number, R is radiation parameter, Ec is Eckert number, Q is heat generation parameter, and L is velocity slip parameter.

Another important aspect in this formulation is the quantities of interest for skin friction coefficient $\mathrm{Re}_x^{1/2}C_f$ and the local Nusselt number $\mathrm{Re}_x^{-1/2}Nu_x$. In most technical sectors, determining these quantities helps in analyzing and improving system performance by providing a better understanding of fluid behavior and thermal management efficiency. The quantities of interest are further introduced by [17]

$$C_f = \frac{\mu_{thnf}}{\rho_f u_w^2(x)}\left(\frac{\partial u}{\partial y}\right)\bigg|_{y=0},\ Nu_x = \frac{k_{thnf}}{k_f[T_w(x) - T_\infty]}\left(-\frac{\partial T}{\partial y}\right)\bigg|_{y=0} \tag{12}$$

and we simplified Eq. (12) with Eq. (5) so we achieve

$$\mathrm{Re}_x^{1/2}C_f = \frac{\mu_{thnf}}{\mu_f}f''(0),\ \mathrm{Re}_x^{-1/2}Nu_x = -\left(\frac{k_{thnf}}{k_f} + \frac{4}{3}R\right)\theta'(0) \tag{13}$$

where $\mathrm{Re}_x = \frac{u_w(x)x}{\nu_f}$ is the local Reynolds number.

2.3 Analytical Solution for the Momentum Equation

In this section, analytical solution is presented as a benchmark to support the numerical findings for ternary nanofluid flow over a nonlinear permeable shrinking sheet. This solution provides an explicit form of velocity and temperature profiles that serve as a reference case. Such a closed-form result is valuable for validating the accuracy and stability of the numerical approach, see Maranna et al. [34] and Lone et al. [35]. The derivation was made possible by introducing simplifying assumptions: the flow is steady and laminar, the base fluid and nanoparticles possess constant thermophysical properties, viscous dissipation is neglected, and velocity slip is approximated up to the first-order term. These assumptions reduce the nonlinear system to a tractable form suitable for analytical treatment.

By disregarding specific parameters such as φ_i for $i = 1, 2, 3$, while we set $M = 0$ and $m = 1$, the BVP in Eq. (8) can simplify to

$$\begin{gathered} f''' - (f\prime)^2 + ff'' = 0 \\ f(0) = S,\ \ f\prime(0) = \Gamma + Lf''(0),\ \ f\prime(\eta) \to 0 \text{ as } \eta \to \infty \end{gathered} \tag{14}$$

which corresponds to the classical case of a viscous fluid. This particular form of the equation is known to admit an exact analytical solution at [36]

$$f(\eta) = S + \frac{\Gamma}{\alpha + \alpha^2 L}\left[1 - \exp(-\alpha\eta)\right] \tag{15}$$

Here, α represents the effective distance parameter. For the solution to be physically relevant, α must be positive ($\alpha > 0$), which ensures the potential existence of multiple solutions. By description, analytical solution based on the boundary layer equations provides meaningful outcomes especially in cases where numerical methods may introduce approximation errors. However, obtaining closed-form solutions is often limited to simplified cases with reduced governing equations. In practical scenarios involving complex fluid interactions, numerical approaches become essential for capturing the full range of physical effects and since it produces velocity and temperature profiles that converge with the boundary conditions, only one root of α is retained in the formulation. Alternative roots give rise to unbounded or non-physical behaviors, which are not consistent with the flow system under consideration. The retained root therefore ensures that the analytical solution functions as a reliable comparison for the numerical results. Hence, by substituting Eq. (15) into Eq. (14), we obtain

$$\alpha^2 - \alpha S - \Gamma = 0 \tag{16}$$

Table 3 Comparison of $f''(0)$ against suction parameter S

S	$f''(0)$	
	Mishra et al. [30]	Current analysis
− 0.7	− 0.7111	− 0.7110142
− 0.4	− 0.8214	− 0.8214379
0.0	− 1.0014	− 1.0013901
0.5	− 1.2207	− 1.2206877
0.7	− 1.4099	− 1.4099816

where

$$\alpha = \frac{S + \sqrt{S^2 + 4\Gamma}}{2} \tag{17}$$

so it leads to the expected result that $\Gamma_c = -\frac{S^2}{4}$, where $\Gamma_c < 0$ represents the critical value of Γ beyond which the BVP in Eq. (14) has no practical solutions. Furthermore, by setting $\Gamma = 1$ and $S = 0$, Eq. (15) can simplify to $f''(0) = -1$. This result is consistent with the classical solution initially presented by Crane et al. [37] for boundary layer flow induced by a stretching sheet. The values of $f''(0)$ are then computed with different numbers of S, which listed accordingly in Table 3.

2.4 Analytical Solution for the Energy Equation

For the analytical solution, the problem is simplified by considering the case where the nanoparticle fractions ($\varphi_{1,2,3} = 0.0$) and all other parameters are absent. Under these conditions, the BVP in Eq. (9) reduces to

$$\begin{gathered} \theta'' + \Pr f\theta\prime = 0 \\ \theta(0) = 1,\ \ \theta(\eta) \to 0 \text{ as } \eta \to \infty \end{gathered} \tag{18}$$

which represents the temperature profiles in the absence of additional thermal effects. The corresponding analytical solution is given by

$$\theta(\eta) = 1 - \left(\frac{\int_0^h \Pr f \, dh}{\int_0^\infty \Pr f \, d\eta} \right) \tag{19}$$

where Eq. (19) satisfies the governing equation under these simplified conditions. The heat transfer rate $-\theta'(0)$ is then determined from this solution so that

$$-\theta\prime(0) = \frac{1}{\int_0^\infty \Pr f \, d\eta} \tag{20}$$

To ensure accuracy, computed values of $-\theta\prime(0)$ for different Prandtl numbers *Pr* are compared between numerical

Table 4 Comparison of numerical and analytical solutions for the $-\theta\prime(0)$

Pr	$-\theta\prime(0)$		Khan and Pop [38]	Wang [39]
	Solution from Eq. (18)	Solution from Eq. (20)		
2	0.911358	0.911358	0.911	0.911
7	1.895404	1.895403	1.895	1.895
20	3.353912	3.356904	3.354	3.354
70	6.462249	6.462199	6.462	6.462

solution from Eq. (18) and analytical solution from Eq. (20) as listed in Table 4. For consistency in comparison, the analysis is conducted by setting $\varphi_1 = \varphi_2 = \varphi_3 = 0.0$ and neglecting the effects of Eckert number Ec, magnetic field M, and radiation parameter R. The close agreement between the obtained results and previous studies confirms the reliability of both the numerical and analytical approaches.

3 Numerical Results

The results in this research are based on the mathematical models described in Eqs. (8)–(10), which were solved using a finite difference approach through bvp4c scheme in MATLAB software. This scheme applies the three-stage collocation method of Lobatto-IIIa approach per subinterval. The accuracy of the numerical solution for the BVPs in Eqs. (8)–(10) relies on this method [40]. The plot of skin friction coefficient $\mathrm{Re}_x^{1/2} C_f$ and Nusselt number $\mathrm{Re}_x^{-1/2} Nu_x$ for three nanofluids: mono, hybrid, and ternary, is presented in Fig. 3. It was observed that two solutions exist within the range $\Gamma_c \leq \Gamma < 0$, with ternary nanofluid showing the widest range of dual solutions. Over a shrinking surface, the fluid flow can develop two different solutions when the shrinking parameter Γ reaches certain critical values: (i) the first solution—generally stable and linked to higher wall shear stress, and (ii) the second solution—often unstable and associated with lower shear stress, which justify by Ahmed et al. [41].

The presence of the lower (second) solution is not only a mathematical justification but also carries physical interpretation. Although typically unstable, the lower solution signals the boundary between sustained flow and flow breakdown. Recognizing the existence of the lower solution helps to define the limits of operational stability, since exceeding these conditions may push the system into a non-physical regime where the boundary layer detaches [42]. As Γ approaches a critical limit, two possible flow behaviors occurred prior to the bifurcation process on the boundary layer. When this threshold is exceeded, real solutions no longer exist, suggesting that the flow cannot sustain itself and may experience separation [43]. In practical systems, such bifurcation behavior is linked to operating limits where stable and unstable flow regimes coexist. For example, in electronic cooling systems, reaching a bifurcation point may cause boundary layer detachment and this leads to reduced heat transfer efficiency and increased drag. Operating near such thresholds also can result in unstable heat dissipation which potentially triggering overheating or performance loss. Therefore, identifying the critical parameter ranges associated with bifurcation helps engineers design systems that avoid unstable regimes [44]. Figures 4, 5, 6 then present the effects of the nonlinearity parameter m, magnetic parameter M, radiation parameter R, and heat generation parameter Q, accordingly, where the range of dual solutions can further be observed.

Further, two profiles of velocity $f\prime(\eta)$ and temperature distribution $\theta(\eta)$ with shrinking parameter Γ are presented in Fig. 7, where we notice the increase in Γ parameter significantly increases velocity profiles $f\prime(\eta)$. As Γ increases, the shrinking effect intensifies and causing the flow domain to contract more rapidly. This contraction generates a stronger shrinking effect on the fluid near the sheet which increases the flow velocity. Simultaneously, the increased Γ contributes to a thinner boundary layer. This reduces the thermal diffusion from the sheet to the surrounding fluid. This effect, combined with the radiative cooling influence, results in a decrease in the first solution of temperature profiles $\theta(\eta)$. The work between the momentum and thermal boundary layers under the combined effects of radiation and the ternary nanoparticles further amplifies these trends. Figure 8 then depicts the profiles of $f\prime(\eta)$ and $\theta(\eta)$ against slip parameter L. From Fig. 8a, a declining pattern of both solutions in $f\prime(\eta)$ can be attributed to the reduced resistance against the wall when L increases, which allowing it to slip more easily rather than adhering closely to the boundary. In terms of temperature profiles $\theta(\eta)$, the first solution is shown to increase probably due to the fluid near the wall does not carry away heat as efficiently with less frictional force at the boundary. Although the addition of three nanoparticles could generally enhance thermal conductivity, the reduced boundary layer friction due to higher slip limits the effectiveness of heat transfer at the surface.

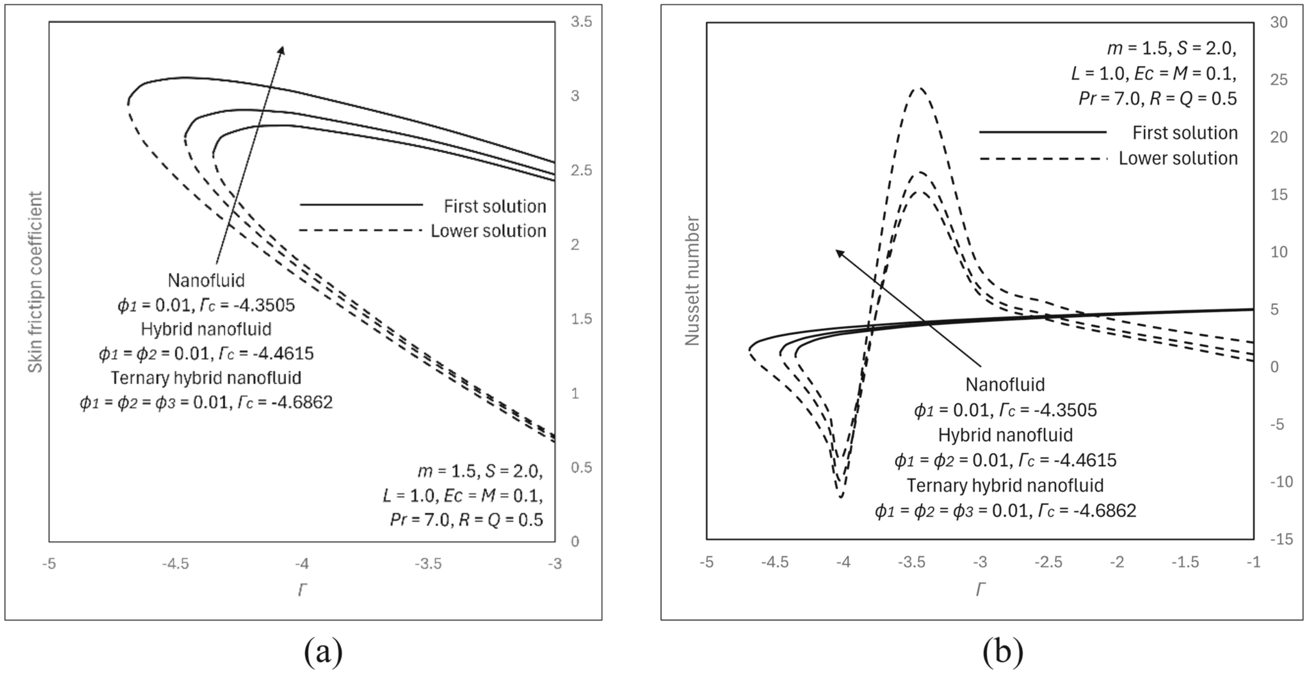

Fig. 3 Three types of nanofluids against **a** $\mathrm{Re}_x^{1/2} C_f$, and **b** $\mathrm{Re}_x^{-1/2} Nu_x$

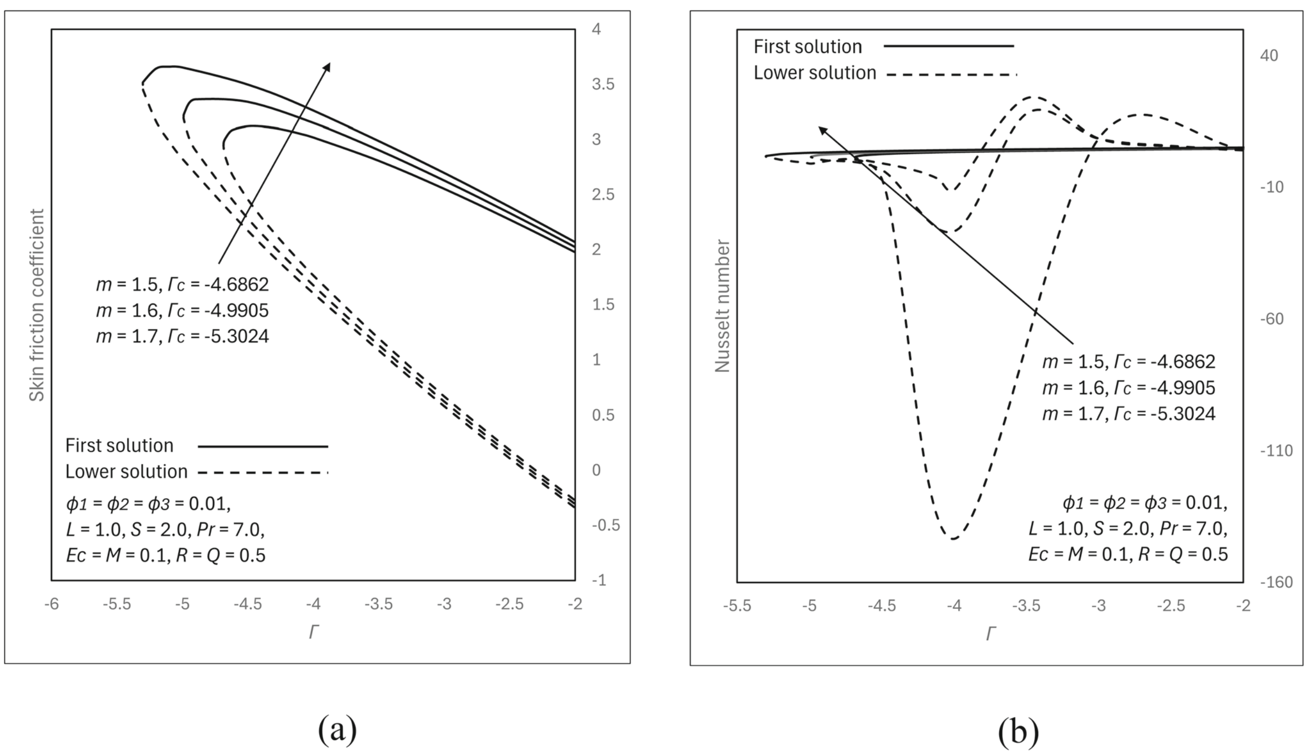

Fig. 4 Nonlinearity parameter m against **a** $\mathrm{Re}_x^{1/2} C_f$, and **b** $\mathrm{Re}_x^{-1/2} Nu_x$

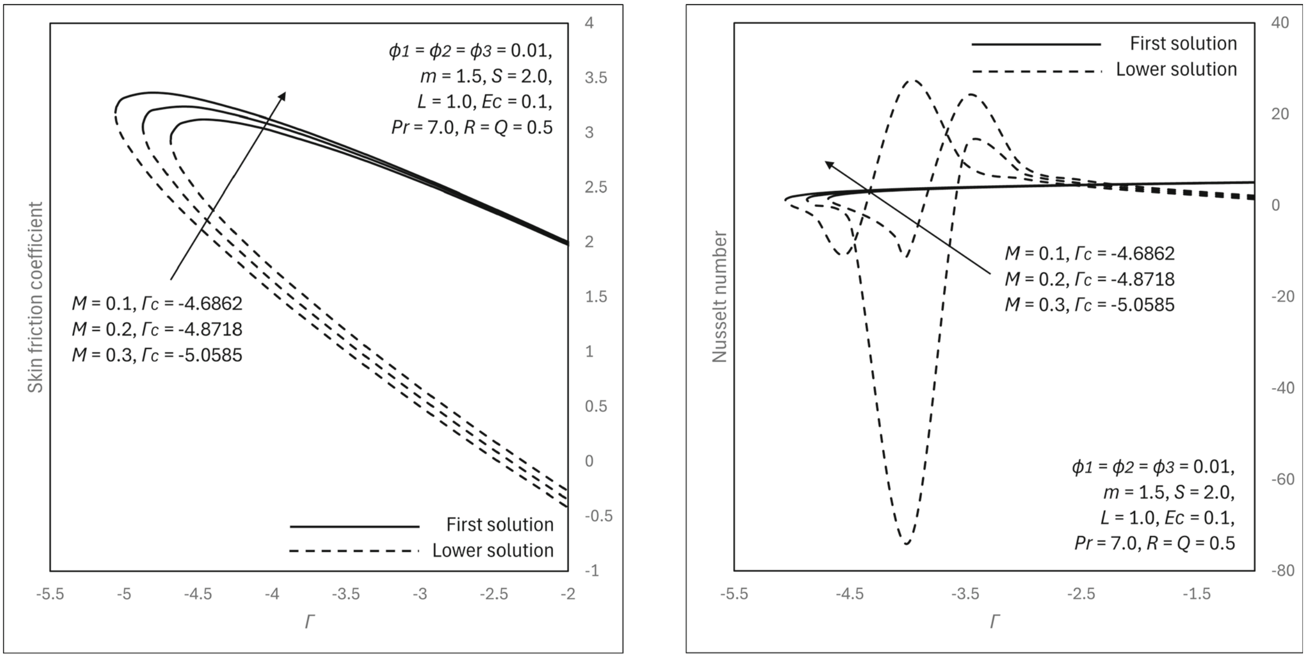

(a) (b)

Fig. 5 Magnetic parameter M against **a** $\mathrm{Re}_x^{1/2} C_f$, and **b** $\mathrm{Re}_x^{-1/2} Nu_x$

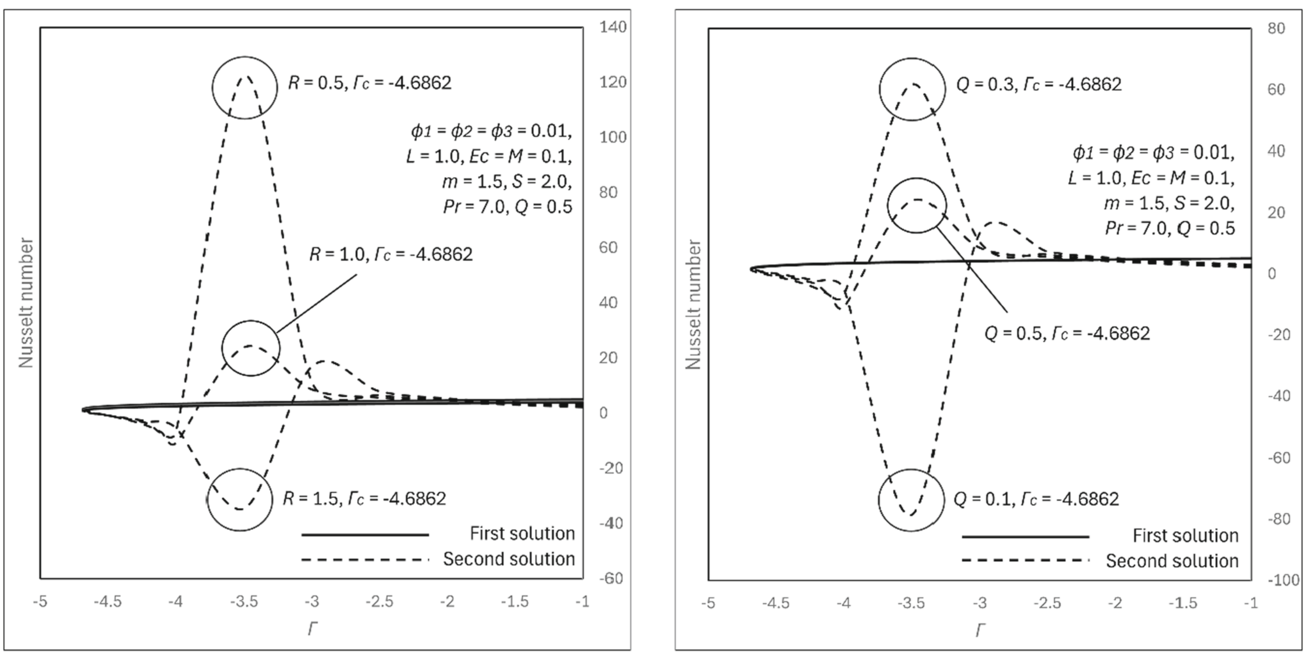

(a) (b)

Fig. 6 $\mathrm{Re}_x^{-1/2} Nu_x$ against parameter of **a** radiation R, and **b** heat generation Q

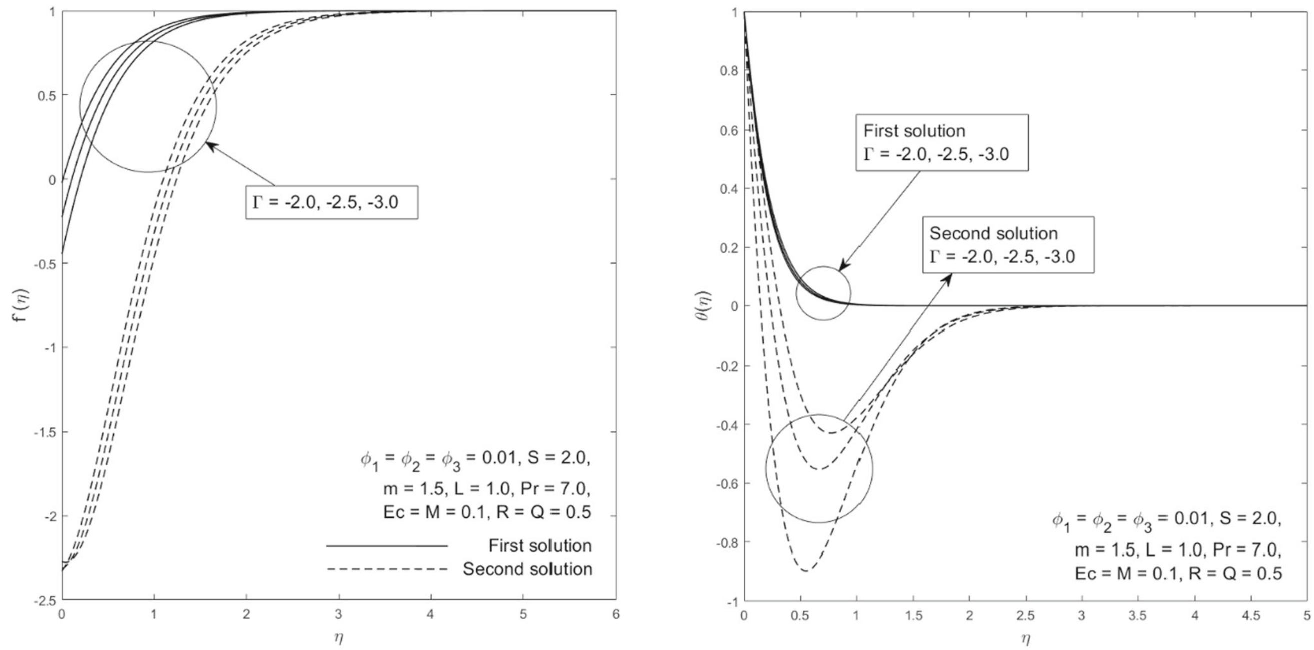

(a) (b)

Fig. 7 Shrinking parameter Γ against **a** $f'(\eta)$, and **b** $\theta(\eta)$

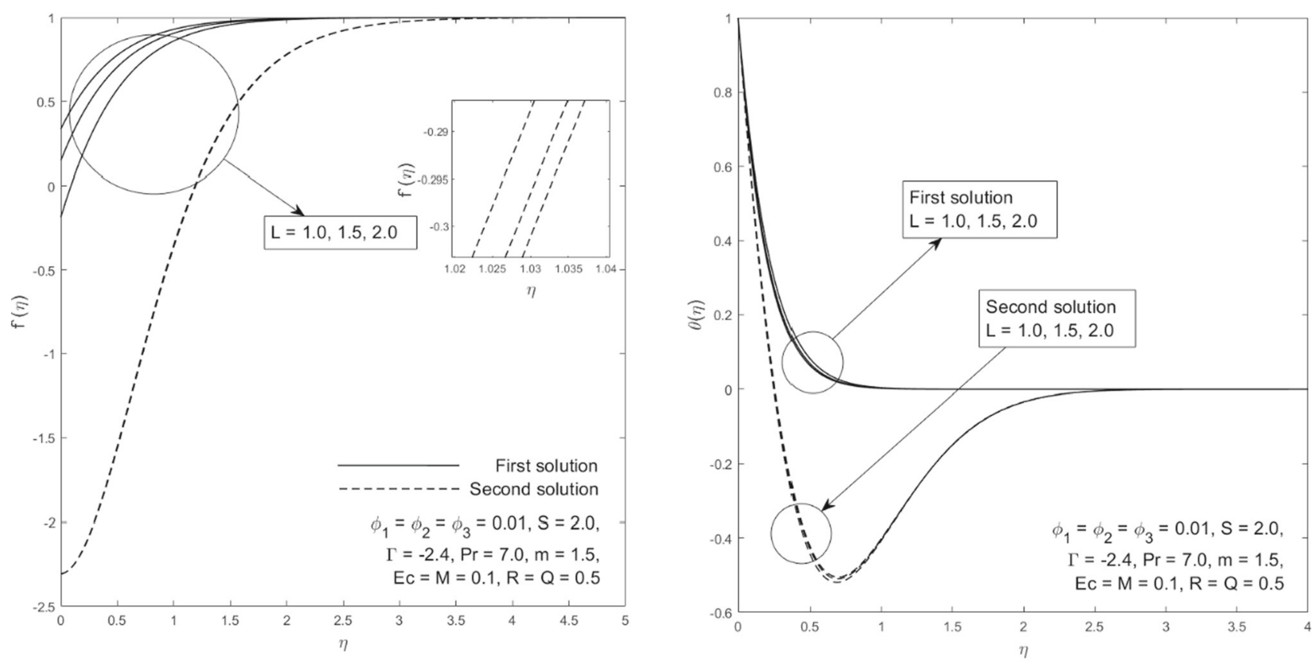

(a) (b)

Fig. 8 Velocity slip parameter L against **a** $f'(\eta)$, and **b** $\theta(\eta)$

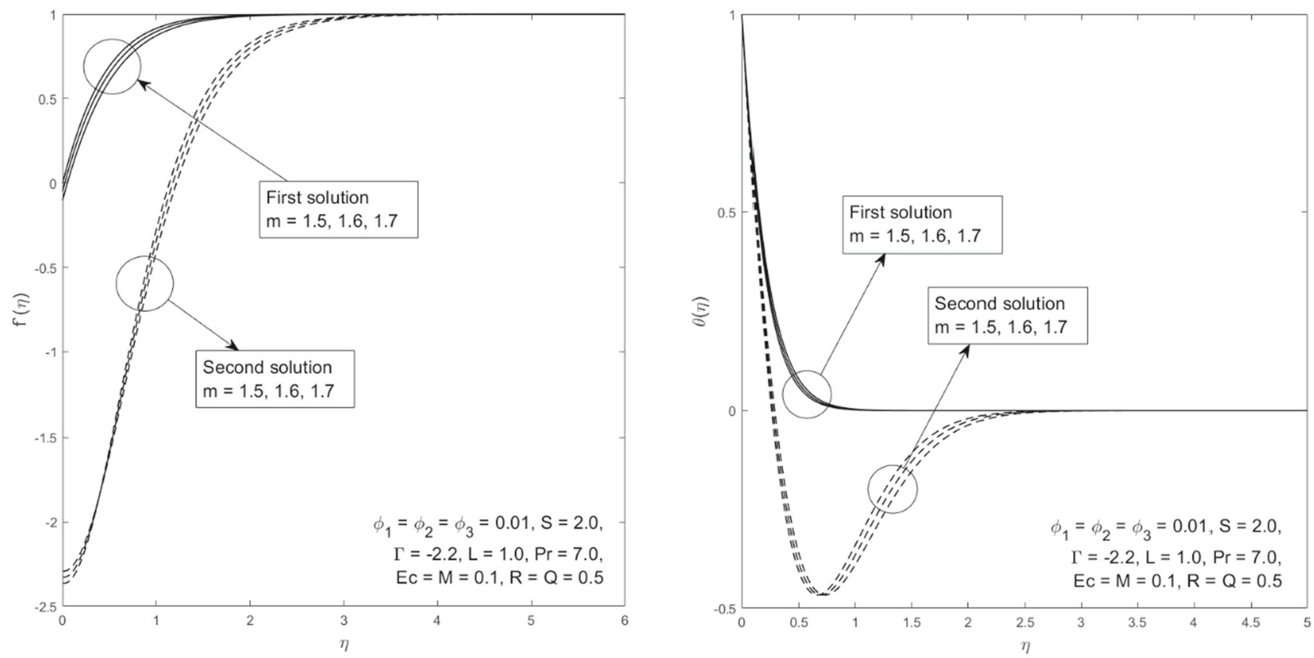

(a) (b)

Fig. 9 Nonlinearity parameter m against **a** $f'(\eta)$, and **b** $\theta(\eta)$

The effect of nonlinearity parameter m on both profiles of $f\prime(\eta)$ and $\theta(\eta)$ is visualized in Fig. 9. By definition, the stretching or shrinking behavior of the sheet becomes more pronounced in a nonlinear manner when m increases, which in turns enhances the fluid's momentum near the surface. This leads to an increase in the first solution of $f\prime(\eta)$ because the fluid is being 'pulled' or 'pushed' more strongly by the surface's nonlinear behavior. Simultaneously, when m increases, it alters the shrinking rate along the sheet which introduces a spatially varying effect that can enhance fluid motion near certain regions of the sheet. This variation impacts the temperature distribution $\theta(\eta)$ as displayed in Fig. 9b. Additionally, the nonlinear nature from the shrinking sheet may lead to changes in the thermal gradients and allowing more heat to accumulate within the fluid near the sheet. Further, Fig. 10 shows the $f\prime(\eta)$ and $\theta(\eta)$ against magnetic parameter M where the second solution of the velocity profiles $f\prime(\eta)$ are shown to decrease. When the magnetic parameter M increases, the Lorentz force that arises from the interaction of the fluid's motion with the imposed magnetic field becomes stronger. This force acts as a resistive drag and opposes the flow motion, which generates the velocity of the nanofluid to decrease across the boundary layer. Based on the temperature profiles $\theta(\eta)$ in Fig. 10b, this suppression of fluid motion indirectly impacts the thermal profile as well. The reduced velocity weakens convective heat transfer within the boundary layer. With diminished convective effects, the thermal diffusion process dominates, causing a reduction in the overall temperature distribution as observed in the second solution.

Figure 11 then displays the effect of thermal radiation parameter R and heat generation parameter Q on temperature profiles $\theta(\eta)$, where the results show that mixed behaviors attended on the solutions against R, while Q parameter tends to dejecting $\theta(\eta)$. For the second solution in Fig. 11a, R parameter enhances the profiles of $\theta(\eta)$ by increasing the thermal energy emitted from the surface and raising the heat transfer to the surrounding fluid. This radiative heat flux contributes to additional energy and leads to a higher thermal boundary thickness. Conversely, the heat generation parameter Q represents as a negative source term in the energy equation, which implies that energy is being dissipated rather than supplied. The effect of this constantly lowering the overall temperature distribution within the nanofluid flow. From an application perspective, these findings are relevant for systems that related with thermal control. An increase in R can be advantageous in high-temperature furnaces, as such, where stronger radiative transfer enhances heat extraction from surfaces. On the other hand, heat generation can reduce temperature distribution in the high-temperature furnaces because internal heat sources need to be controlled to prevent excessive temperature rise.

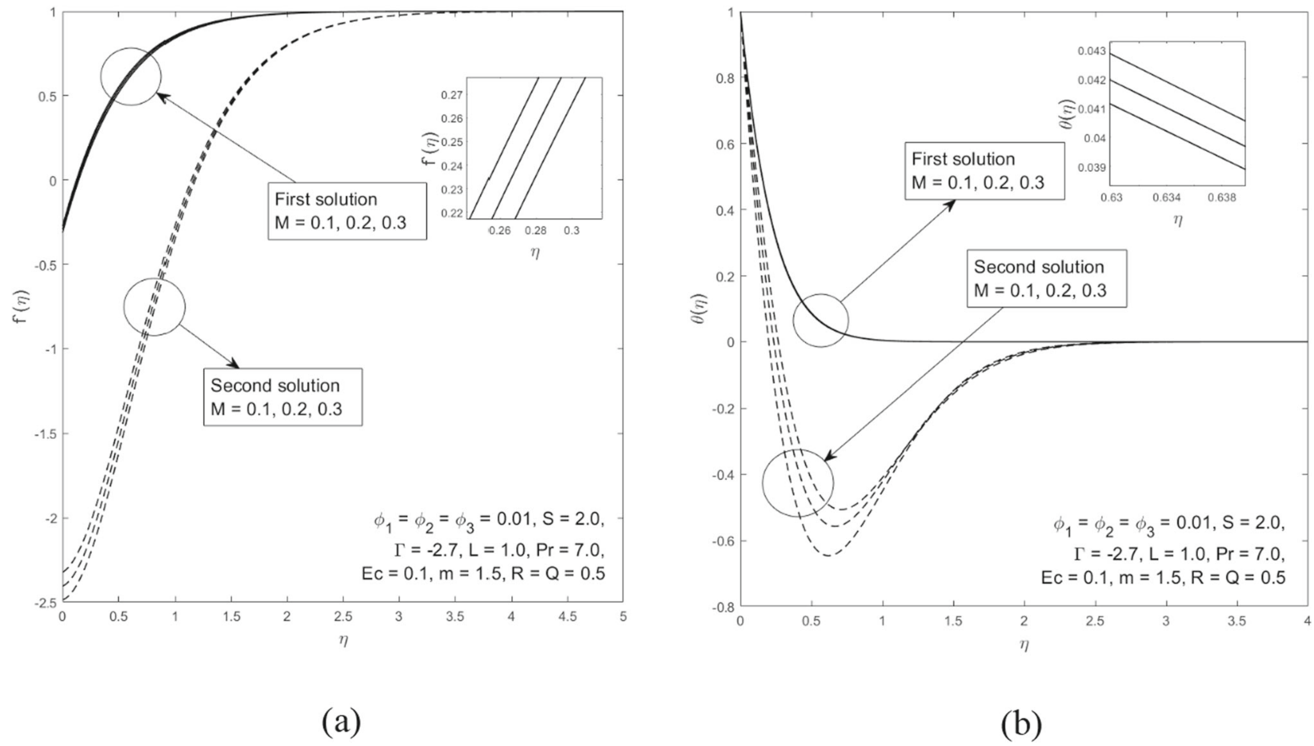

Fig. 10 Magnetic parameter M against **a** $f'(\eta)$, and **b** $\theta(\eta)$

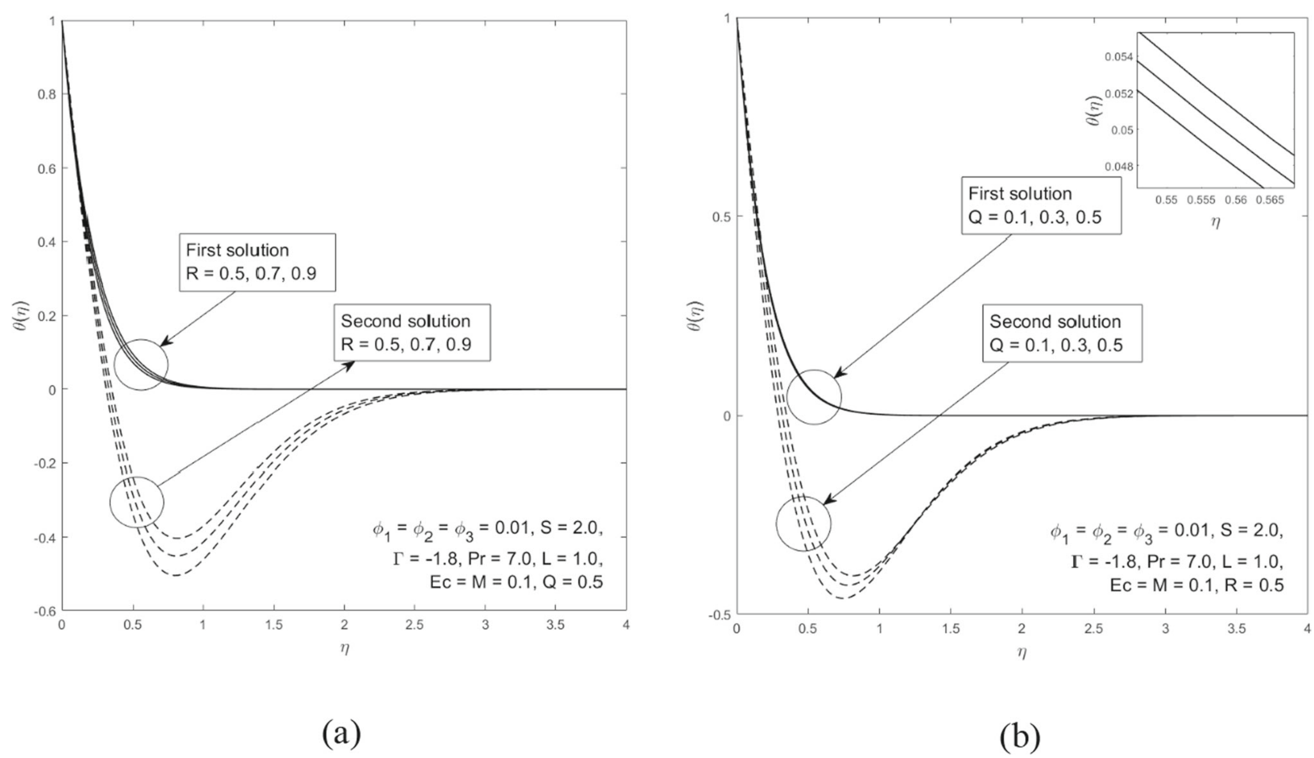

Fig. 11 $\theta(\eta)$ against parameter of **a** radiation R, and **b** heat generation Q

Table 5 Setting of level for three parameters

Parameter	Coded parameter	Level		
		− 1 (Low)	0 (Medium)	1 (High)
m	X	1.5	1.6	1.7
R	Y	0.5	0.7	0.9
Q	Z	0.1	0.2	0.3

4 Optimization of Heat Transfer Rate by RSM

Based on the numerical analysis obtained, optimization using Response Surface Methodology (RSM) is conducted to identify three parameters that significantly influence the response and to determine their optimal levels. RSM is a collection of statistical and mathematical tools designed to model and analyze problems where the response is affected by multiple variables. Introduced by Box and Wilson in the 1950s [45], the goal of RSM is usually to optimize (minimizing or maximizing) the response as this method is further widely used in engineering, manufacturing, and scientific research to improve processes and design experiments efficiently. Visualization tools such as contour plots and three-dimensional surface plots are integral to RSM to provide insights between the variables and their combined effects on the response. Over the years, RSM has been widely adopted in dynamics studies across various fields such as by Wang et al. [46] and Abu Bakar et al. [47]. The core idea of RSM is to approximate the true relationship between input variables and the response using polynomial equations, typically quadratic, and to identify optimal operating conditions, which the general equation for a second-order polynomial model in RSM is given by [48]

$$response = \gamma_0 + \sum_{i=1}^{n} \gamma_i x_i + \sum_{i=1}^{n} \gamma_{ii} x_i^2 + \sum_{i<j}^{n} \gamma_{ij} x_i x_j + E \tag{21}$$

where *res* is the response variable, x_i is the input variables, γ_0 is the intercept, γ_i, γ_{ii}, and γ_{ij} are the coefficients, respectively, and E represents the error coefficient.

In this RSM analysis, three parameters of nonlinearity m, radiation R, and heat generation$Q$ are selected to maximize the heat transfer rate $\mathrm{Re}_x^{-1/2} Nu_x$ (response) while other parameters are fixed at $\varphi_1 = \varphi_2 = \varphi_3 = 0.01$, $S = 2.0$, $\Gamma = -2.0$, $L = 0.1$, and $Ec = M = 0.5$. Table 5 is then presented a detailed overview of these parameters, including their coded values and levels. Additionally, Table 6 lists the experimental design for the RSM analysis.

RSM is occupied to analyze the developed mathematical model, with the results summarized in Table 7 are based on ANOVA analysis. According to Jain et al. [49], a variable term is statistically insignificant when its p-value exceeds 0.05. For the initial model predicting the response $\mathrm{Re}_x^{-1/2} Nu_x$, the term Z^2 were identified as insignificant and excluded from the model due to its high p-values. Following these adjustments, the revised correlations for uncoded and coded coefficients derived from Eq. (21) are now presented in an updated form of

i. Uncoded equation:

$$response = \begin{cases} 0.9581 + 3.561m - 1.0033R - 0.5555Q - 0.2714m^2 + \\ 0.43204R^2 - 0.5945mR + 0.1501mQ + 0.0274RQ \end{cases} \tag{22}$$

ii. Coded equation:

$$response = \begin{cases} 4.745 + 0.231X - 0.269Y - 0.029Z - 0.003X^2 + \\ 0.017Y^2 - 0.012XY + 0.002XZ + 0.0005YZ \end{cases} \tag{23}$$

Figure 12 then presents the residual analysis, including the Normal Probability Plot, Histogram, Versus Fits, and Versus Order plots. These visualizations verify that the model assumptions—normality, independence, and homoscedasticity of residuals—are met, which confirms the validity of the regression model. Meanwhile, Fig. 13 displays the contour and surface plots for the response $\mathrm{Re}_x^{-1/2} Nu_x$, which offering a visual representation of the relationship between the variables of m, R and Q parameters and the response. The plot indicates that optimal parameter values for maximizing the $\mathrm{Re}_x^{-1/2} Nu_x$ are $m = 1.7$ (highest number), $R = 0.5$ (lowest number), and $Q = 0.1$ (lowest number). These optimal values are further validated by six alternative combinations as outlined in Table 8 as the RSM analysis confirms that the highest value of m, and lowest values of R and Q achieve a maximum heat transfer rate $\mathrm{Re}_x^{-1/2} Nu_x$ with a suggested desirability of 99.98%.

5 Conclusions

This study examines the steady, two-dimensional, incompressible flow of a ternary nanofluid Al_2O_3–Cu–TiO_2/H_2O

Table 6 Experimental design for $\mathrm{Re}_x^{-1/2} Nu_x$

Runs	X (m)	Y (R)	Z (Q)	Response ($\mathrm{Re}_x^{-1/2} Nu_x$)
1	− 1	− 1	− 1	4.81767
2	1	− 1	− 1	5.29996
3	− 1	1	− 1	4.30270
4	1	1	− 1	4.73755
5	− 1	− 1	1	4.75424
6	1	− 1	1	5.24265
7	− 1	1	1	4.24158
8	1	1	1	4.68232
9	− 1	0	0	4.51258
10	1	0	0	4.97269
11	0	− 1	0	5.03149
12	0	1	0	4.49378
13	0	0	− 1	4.77469
14	0	0	1	4.71564
15	0	0	0	4.74530
16	0	0	0	4.74530
17	0	0	0	4.74530
18	0	0	0	4.74530
19	0	0	0	4.74530
20	0	0	0	4.75430

Table 7 ANOVA analysis for the response

Source	Deg. of freedom	Adjusted sum square	Adjusted mean square	F-value	*p*-value
Model	8	1.26569	0.158212	1,864,153.99	0.000
Linear	3	1.26329	0.421098	4,961,651.51	
X	1	0.53195	0.531951	6,267,792.32	
Y	1	0.72257	0.722574	8,513,833.71	
Z	1	0.00877	0.008770	103,328.50	
Square	2	0.00125	0.000624	7356.46	
X^2	1	0.00002	0.000024	277.72	
Y^2	1	0.00096	0.000956	11,260.66	
2-Way Interaction	3	0.00115	0.000384	4521.49	
XZ	1	0.00113	0.001131	13,323.75	
YZ	1	0.00002	0.000018	212.36	
ZZ	1	0.00000	0.000002	28.35	
Error	11	0.00000	0.000000		
Lack-of-Fit	6	0.00000	0.000000	*	*
Pure Error	5	0.00000	0.000000		
Total	19	1.26570			

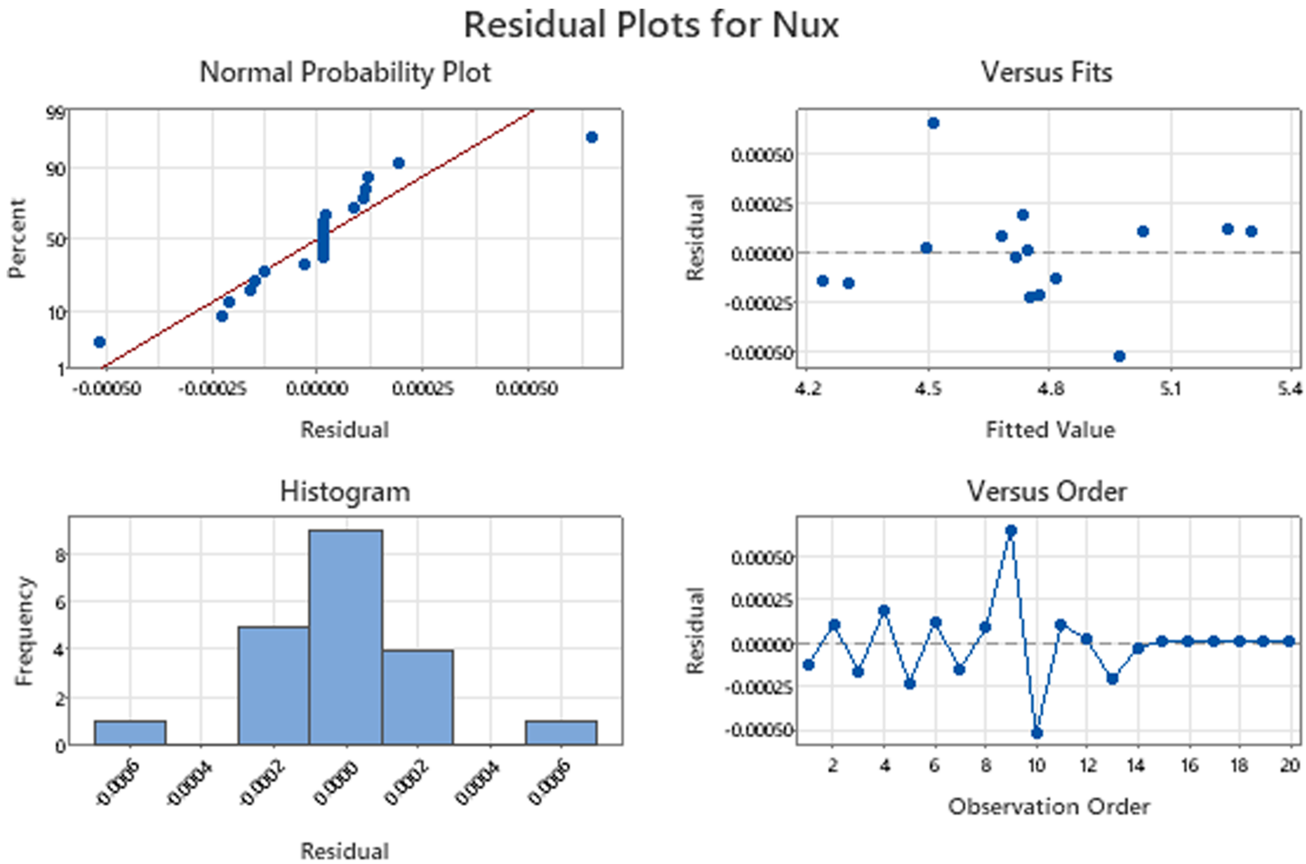

Fig. 12 Residual analysis for the response

flow over a nonlinear impermeable shrinking sheet with velocity slip, radiation, magnetohydrodynamics, and heat generation. The formulation of mathematical model starts with the partial differential form, which are transformed into ordinary differential equations using a similarity transformation method. The numerical solutions are obtained using bvp4c function in MATLAB. Additionally, Response Surface Methodology (RSM) is applied to determine optimal conditions for maximizing the heat transfer rate by selecting key parameters. The findings from the numerical and statistical analysis are summarized as follows:

i. A comparison with previously published results shows strong agreement, verifying the accuracy of the present model.
ii. Multiple flow behaviors are observed based on shrinking parameter $\Gamma < 0$, which presenting two branches of solutions.
iii. The ternary nanofluid achieves higher heat transfer performance compared to both conventional and hybrid nanofluids.
iv. The temperature profiles show varying trends depending on the magnetic parameter M, shrinking parameter Γ, and radiation parameter R. Heat generation parameter Q reduces the temperature, whereas the nonlinearity parameter m increases it.
v. The optimization using RSM shows that the highest heat transfer rate is obtained when the nonlinearity parameter m is maximized, while R and Q are minimized, with a desirability of 99.98%.

Here, this research contributes to the ongoing study on ternary nanofluids by providing both numerical and statistical understandings, which also brings the novelty that is reflected in the simultaneous consideration of the nonlinearity parameter, radiation parameter, and heat generation parameter under a ternary nanofluid model. Although this work is limited to a theoretical and numerical framework, the potential future research could consider the effects of different nanoparticle shapes, dynamic viscosity models, and unsteady flow conditions. In addition, experimental validation of the findings would help bridge the gap between theoretical and real-world applications, particularly in cooling technologies where effective heat dissipation is critical to maintain optimal performance and prevent overheating. Current findings from this work suggest that the model of nonlinear shrinking surface in ternary nanofluids combined

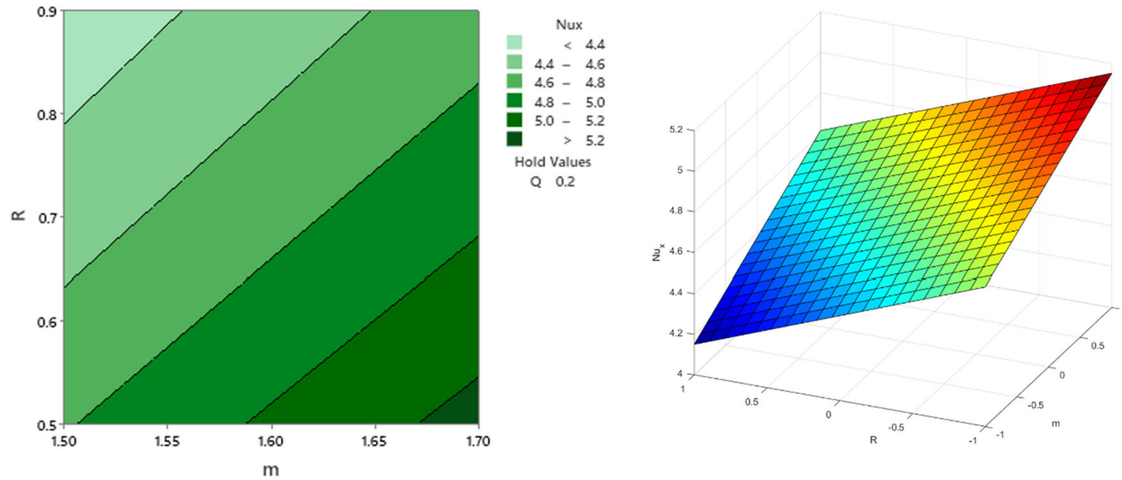

(a) Combination of m and R

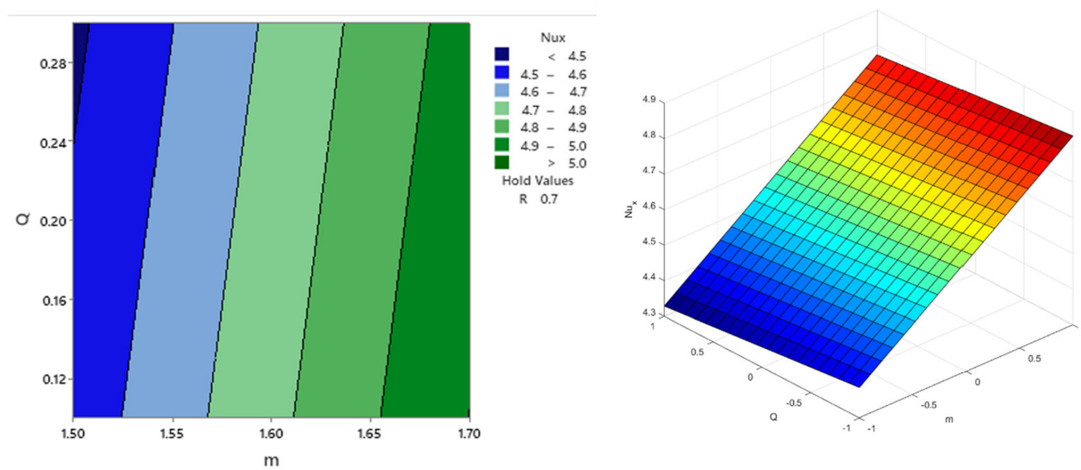

(b) Combination of m and Q

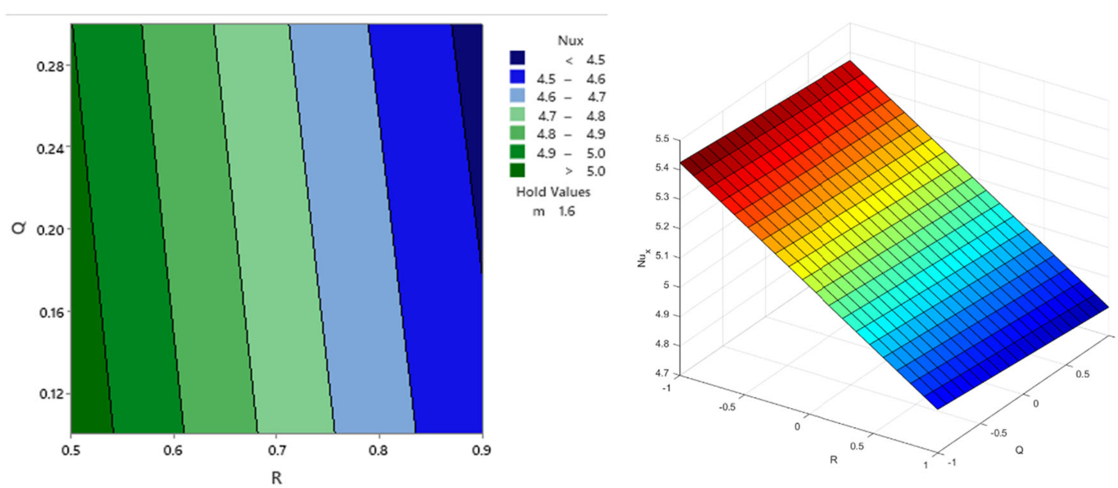

(c) Combination of R and Q

Fig. 13 Contour and surface plots for the response

Table 8 Suggestion of parameters to maximize the response

Solution	*m*	*R*	*Q*	Response fit	Composite desirability
1	1.70000	0.50000	0.10000	5.29985	99.989%
2	1.70000	0.50000	0.29895	5.24283	94.602%
3	1.70000	0.55136	0.10000	5.21990	92.435%
4	1.54277	0.50000	0.10000	4.92271	64.356%
5	1.54864	0.50000	0.29383	4.87707	60.043%
6	1.70000	0.78854	0.29375	4.82621	55.238%
7	1.50000	0.90000	0.10000	4.30286	5.789%

with optimized parameter settings can be applied to achieve higher energy efficiency and prevent overheating in practical engineering designs, such as high-performance battery systems or thermal sensors in electronic devices.

Acknowledgements The resources and facilities for this research were provided by Takasago Thermal Engineering Co. Ltd. Japan (TTE) and Universiti Teknologi Malaysia (UTM), for which the authors express their sincere appreciation.

Author Contributions S.A.B. – formal analysis, methodology, visualization, writing. N.S.W. – formal analysis. N.M.A. – validation. I.P. – conceptualization, methodology.

Funding Open access funding provided by The Ministry of Higher Education Malaysia and Universiti Teknologi Malaysia. This research is funded by Takasago Thermal Engineering Co. Ltd. Japan (TTE) through Grant number R.K130000.7343.1U045.

Data Availability Not available.

Declarations

Conflict of interest They further state that no personal affiliations or conflicts of interest have affected the content of this manuscript.

Ethical Approval The final version of this manuscript has been reviewed and approved by the authors.

References

1. Choi, S.U.; Eastman, J.A.: Enhancing thermal conductivity of fluids with nanoparticles (No. ANL/MSD/CP-84938; CONF-951135-29). Argonne National Lab.(ANL), Argonne, IL (United States) (1995)
2. Huminic, G.; Huminic, A.: Hybrid nanofluids for heat transfer applications–a state-of-the-art review. Int. J. Heat Mass Transf. **125**, 82–103 (2018). https://doi.org/10.1016/j.ijheatmasstransfer.2018.04.059
3. Mohanty, D.; Mahanta, G.; Shaw, S.: Irreversibility and thermal performance of nonlinear radiative cross-ternary hybrid nanofluid flow about a stretching cylinder with industrial applications. Powder Technol. **433**, 119255 (2024). https://doi.org/10.1016/j.powtec.2023.119255
4. Parida, C.; Lekgari, M.V.; Mahanta, G.; Shaw, S.: Multi-layer neural network on 3D transition metal hydrides-based ternary nanofluid flow with entropy: application to spinning disc reactor. Therm. Sci. Eng. Prog. (2025). https://doi.org/10.1016/j.tsep.2025.103641
5. Nath, R.S.; Deka, R.K.: A numerical investigation of the MHD ternary hybrid nanofluid (Cu-Al2O3-TiO2/H2O) past a vertically stretching cylinder in a porous medium with thermal stratification. J. Adv. Res. Fluid Mech. Therm. Sci. **116**(1), 78–96 (2024). https://doi.org/10.37934/arfmts.116.1.7896
6. Takreem, M.; Pv, S.N.: Impact of Cattaneo-Christov heat flux on mixed convection flow of a ternary hybrid (Cu-Al2O3-TiO2/H2O) nanofluid over an elongated sheet: a comparative analysis. Indian J. Chem. Technol. (IJCT) **31**(1), 57–69 (2024). https://doi.org/10.56042/ijct.v31i1.3263
7. Mahmood, Z.; Ahammad, N.A.; Alhazmi, S.E.; Khan, U.; Bani-Fwaz, M.Z.: Ternary hybrid nanofluid near a stretching/shrinking sheet with heat generation/absorption and velocity slip on unsteady stagnation point flow. Int. J. Mod. Phys. B **36**(29), 2250209 (2022). https://doi.org/10.1142/S0217979222502095
8. Nasir, S.; Sirisubtawee, S.; Gul, T.; Juntharee, P.; Alghamdi, W.; Ali, I.: Thermal characteristics of nonlinear convection and radiation for the flow of tri-hybrid nanofluids over stretchable surface with energy source. Surf. Rev. Lett. **29**(11), 2250153 (2022). https://doi.org/10.1142/S0218625X22501530
9. Shanmugapriya, M.; Sundareswaran, R.; Kumar, P.S.; Rangasamy, G.: Impact of nanoparticle shape in enhancing heat transfer of magnetized ternary hybrid nanofluid. Sustain. Energy Technol. Assess. **53**, 102700 (2022). https://doi.org/10.1016/j.seta.2022.102700
10. Gohar, S.; Alyami, M.A.; Akkurt, N.; Khan, T.S.; Gul, T.: Ternary hybrid nanofluids flow on a spinning disk with nonlinear thermal radiation. ZAMM Z. Angew. Math. Mech. **103**(5), e202200203 (2023). https://doi.org/10.1002/zamm.202200203
11. Madhukesh, J.K.; Sarris, I.E.; Prasannakumara, B.C.; Abdulrahman, A.: Investigation of thermal performance of ternary hybrid nanofluid flow in a permeable inclined cylinder/plate. Energies **16**(6), 2630 (2023). https://doi.org/10.3390/en16062630
12. Sarangi, M.K.; Thatoi, D.N.; Shaw, S.; Azam, M.; Chamkha, A.J.; Nayak, M.K.: Hydrothermal behavior and irreversibility analysis of Bödewadt flow of radiative and dissipative ternary composite nanomaterial due to a stretched rotating disk. Mater. Sci. Eng. B **287**, 116124 (2023). https://doi.org/10.1016/j.mseb.2022.116124

13. Bachok, N.; Ishak, A.: Similarity solutions for the stagnation-point flow and heat transfer over a nonlinearly stretching/shrinking sheet. Sains Malaysiana **40**(11), 1297–1300 (2011)
14. Hunegnaw, D.; Kishan, N.: MHD boundary layer flow and heat transfer over a non-linearly permeable stretching/shrinking sheet in a nanofluid with suction effect, thermal radiation and chemical reaction. J. Nanofluids **3**(4), 399–407 (2014). https://doi.org/10.1166/jon.2014.1121
15. Zaimi, K.; Ishak, A.; Pop, I.: Boundary layer flow and heat transfer over a nonlinearly permeable stretching/shrinking sheet in a nanofluid. Sci. Rep. **4**(1), 4404 (2014). https://doi.org/10.1038/srep04404
16. Khan, U.; Ahmed, N.; Mohyud-Din, S.T.; Bin-Mohsin, B.: Nonlinear radiation effects on MHD flow of nanofluid over a nonlinearly stretching/shrinking wedge. Neural Comput. Appl. **28**, 2041–2050 (2017). https://doi.org/10.1007/s00521-016-2187-x
17. Waini, I.; Ishak, A.; Pop, I.: Hybrid nanofluid flow and heat transfer over a nonlinear permeable stretching/shrinking surface. Int. J. Numer. Methods Heat Fluid Flow **29**(9), 3110–3127 (2019). https://doi.org/10.1108/HFF-01-2019-0057
18. Lund, L.A.; Omar, Z.; Khan, I.; Sherif, E.S.M.: Dual branches of MHD three-dimensional rotating flow of hybrid nanofluid on nonlinear shrinking sheet. Comput. Mater. Contin. **66**(1), 127–139 (2020). https://doi.org/10.32604/cmc.2020.013120
19. Khan, U.; Zaib, A.; Pop, I.; Waini, I.; Ishak, A.: MHD flow of a nanofluid due to a nonlinear stretching/shrinking sheet with a convective boundary condition: Tiwari-Das nanofluid model. Int. J. Numer. Methods Heat Fluid Flow **32**(10), 3233–3258 (2022). https://doi.org/10.1108/HFF-11-2021-0730
20. Bachok, N.; Tajuddin, S.N.N.; Anuar, N.S.; Rosali, H.: Numerical computation of stagnation point flow and heat transfer over a nonlinear stretching/shrinking sheet in hybrid nanofluid with suction/injection effects. J. Adv. Res. Fluid Mech. Therm. Sci. **107**(1), 80–86 (2023). https://doi.org/10.37934/arfmts.107.1.8086
21. Roy, N.C.; Pop, I.: Dual solutions of a nanofluid flow past a convectively heated nonlinearly shrinking sheet. Chin. J. Phys. **82**, 31–40 (2023). https://doi.org/10.1016/j.cjph.2022.12.008
22. Day, M.A.: The no-slip condition of fluid dynamics. Erkenntnis **33**(3), 285–296 (1990). https://doi.org/10.1007/BF00717588
23. Sahraoui, M.; Kaviany, M.: Slip and no-slip velocity boundary conditions at interface of porous, plain media. Int. J. Heat Mass Transf. **35**(4), 927–943 (1992). https://doi.org/10.1016/0017-9310(92)90258-T
24. Ahmadi, E.; Sadeghi, A.; Chakraborty, S.: Slip-coupled electroosmosis and electrophoresis dictate DNA translocation speed in solid-state nanopores. Langmuir **39**(35), 12292–12301 (2023). https://doi.org/10.1021/acs.langmuir.3c01230
25. Manjunatha, S.; Puneeth, V.; Baby, A.K.; Vishalakshi, C.S.: Examination of thermal and velocity slip effects on the flow of blood suspended with aluminum alloys over a bi-directional stretching sheet: the ternary nanofluid model. Waves Random Complex Media (2022). https://doi.org/10.1080/17455030.2022.2056260
26. Rafique, K.; Mahmood, Z.; Khan, U.; Eldin, S.M.; Oreijah, M.; Guedri, K.; Khalifa, H.A.E.W.: Investigation of thermal stratification with velocity slip and variable viscosity on MHD flow of Al2O3− Cu− TiO2/H2O nanofluid over disk. Case Stud. Therm. Eng. **49**, 103292 (2023). https://doi.org/10.1016/j.csite.2023.103292
27. Sudharani, M.V.V.N.L.; Prakasha, D.G.; Kumar, K.G.; Chamkha, A.J.: Computational assessment of hybrid and tri hybrid nanofluid influenced by slip flow and linear radiation. Eur. Phys. J. Plus **138**(3), 257 (2023). https://doi.org/10.1140/epjp/s13360-023-03852-2
28. Mumtaz, M.; Islam, S.; Ullah, H.; Dawar, A.; Shah, Z.: A numerical approach to radiative ternary nanofluid flow on curved geometry with cross-diffusion and second order velocity slip constraints. Int. J. Heat Fluid Flow **105**, 109255 (2024). https://doi.org/10.1016/j.ijheatfluidflow.2023.109255
29. Bakar, S.A.; Arifin, N.M.; Pop, I.: Mixed convection hybrid nanofluid flow past a stagnation-point region with variable viscosity and second-order slip. J. Adv. Res. Micro Nano Eng. **12**(1), 1–21 (2023). https://doi.org/10.37934/armne.12.1.121
30. Mishra, S.; Swain, K.; Dalai, R.: Joule heating and viscous dissipation effects on heat transfer of hybrid nanofluids with thermal slip. Iran. J. Sci. Technol. Trans. Mech. Eng. **48**(2), 531–539 (2024). https://doi.org/10.1007/s40997-023-00681-7
31. Takabi, B.; Salehi, S.: Augmentation of the heat transfer performance of a sinusoidal corrugated enclosure by employing hybrid nanofluid. Adv. Mech. Eng. **6**, 147059 (2014). https://doi.org/10.1155/2014/147059
32. Ragulkumar, E.; Sambath, P.; Suresh, K.; Balasubramanian, S.; Chamkha, A.J.: Soret–dufour mass transfer effects on radiative chemically dissipative MHD plain convective water nanofluid (Al2O3, Cu, Ag, & TiO2) flow across a temperature-controlled upright cone surface with heat blow/suction. Numer. Heat Transf. A Appl. (2023). https://doi.org/10.1080/10407782.2023.2261624
33. Obalalu, A.M.; Olayemi, O.A.; Salaudeen, S.A.; Adeshola, A.D.; Ojewola, O.B.; Akindele, A.O.; Oladapo, O.A.: Hydrothermal characteristics-based water purification model using hybrid nanofluid flow over non-linearly stretched permeable surfaces. Nano Hybrids Compos. **44**, 53–69 (2024). https://doi.org/10.4028/p-0Qhsjl
34. Maranna, T.; Mahabaleshwar, U.S.; Kopp, M.I.: The impact of Marangoni convection and radiation on flow of ternary nanofluid in a porous medium with mass transpiration. J. Appl. Comput. Mech. **9**(2), 487–497 (2023). https://doi.org/10.22055/jacm.2022.41405.3748
35. Lone, S.A.; Khan, A.; Raiza, Z.; Alrabaiah, H.; Shahab, S.; Saeed, A.; Bonyah, E.: A semi-analytical solution of the magnetohydrodynamic blood-based ternary hybrid nanofluid flow over a convectively heated bidirectional stretching surface under velocity slip conditions. AIP Adv. (2024). https://doi.org/10.1063/5.0201663
36. Usafzai, W.K.; Aly, E.H.; Tharwat, M.M.; Mahros, A.M.: Modeling of micropolar nanofluid flow over flat surface with slip velocity and heat transfer: exact multiple solutions. Alex. Eng. J. **75**, 313–323 (2023). https://doi.org/10.1016/j.aej.2023.06.004
37. Crane, L.J.: Flow past a stretching plate. Z. Angew. Math. Phys. ZAMP **21**, 645–647 (1970). https://doi.org/10.1007/BF01587695
38. Khan, W.A.; Pop, I.: Boundary-layer flow of a nanofluid past a stretching sheet. Int. J. Heat Mass Transf. **53**(11–12), 2477–2483 (2010). https://doi.org/10.1016/j.ijheatmasstransfer.2010.01.032
39. Wang, C.Y.: Free convection on a vertical stretching surface. ZAMM J. Appl. Math. Mech. **69**(11), 418–420 (1989). https://doi.org/10.1002/zamm.19890691115
40. Abu Bakar, S.; Wahid, N.S.; Md Arifin, N.; Pop, I.: Effects of homogenous–heterogenous reactions and hybrid nanofluid on Bödewadt flow over a permeable stretching/shrinking rotating disk with radiation. Arab. J. Sci. Eng. (2024). https://doi.org/10.1007/s13369-024-08909-7
41. Ahmed, S.; Chen, Z.M.; Ishaq, M.: Multiple solutions in magnetohydrodynamic stagnation flow of hybrid nanofluid past a sheet with mathematical chemical reactions model and stability analysis. Phys. Fluids (2023). https://doi.org/10.1063/5.0157429
42. Rafiq, M.Y.; Sabeen, A.; Rehman, A.U.; Abbas, Z.: Comparative study of Yamada-Ota and Xue models for MHD hybrid nanofluid flow past a rotating stretchable disk: stability analysis. Int. J. Numer. Methods Heat Fluid Flow **34**(10), 3793–3819 (2024). https://doi.org/10.1108/HFF-01-2024-0060
43. Bakar, S.A.; Ismail, N.S.; Arifin, N.M.: Hybrid nanofluid flow over a shrinking darcy-forchheimer porous medium with shape factor

and solar radiation: a stability analysis. CFD Lett. **16**(11), 60–81 (2024). https://doi.org/10.37934/cfdl.16.11.6081
44. Yang, J.; Cheng, K.; Zhang, K.; Huang, C.; Huai, X.: Numerical study on thermal and hydraulic performances of a hybrid manifold microchannel with bifurcations for electronics cooling. Appl. Therm. Eng. **232**, 121099 (2023). https://doi.org/10.1016/j.applthermaleng.2023.121099
45. Box, G.E.P.; Wilson, K.B.: Series b (methodological). J. Roy. Stat. Soc. **13**(1), 1–45 (1951)
46. Wang, J.; Khan, S.A.; Yasmin, S.; Alam, M.M.; Liu, H.; Farooq, U.; Akgül, A.; Hassan, A.M.: Central composite design (CCD)-response surface methodology (RSM) for modeling and simulation of MWCNT-water nanofluid inside hexagonal cavity: application to electronic cooling. Case Stud. Therm. Eng. **50**, 103488 (2023). https://doi.org/10.1016/j.csite.2023.103488
47. Abu Bakar, S.; Wahid, N.S.; Md Arifin, N.; Pop, I.: Optimization of heat transfer on Jeffrey ternary nanofluid flow with slip conditions and heat generation by response surface methodology. Multiscale Multidiscip. Model. Exp. Des. **8**(2), 1–17 (2025). https://doi.org/10.1007/s41939-025-00744-z
48. Lamidi, S.; Olaleye, N.; Bankole, Y.; Obalola, A.; Aribike, E.; Adigun, I.: Applications of response surface methodology (RSM) in product design, development, and process optimization. IntechOpen (2022). https://doi.org/10.5772/intechopen.106763
49. Jain, S.; Mishra, R.S.; Mehdi, H.; Gupta, R.; Dubey, A.K.: Optimization of processing variables of friction stir welded dissimilar composite joints of AA6061 and AA7075 using response surface methodology. J. Adhes. Sci. Technol. **38**(6), 949–968 (2024). https://doi.org/10.1080/01694243.2023.2243682